A newly discovered Late-Cretaceous East Asian flat slab explains its unique lithospheric structure and tectonics

Diandian Peng[1*], Lijun Liu[1]

[1] *University of Illinois at Urbana-Champaign, Urbana, IL 61801, USA*

[*] *Correspondence to: dp6@illinois.edu*

Key points:

- Global data-assimilation models reproducing past subduction discovered a previously unrecognized continental-scale flat Izanagi slab.
- The flat Izanagi slab caused the unique East Asian lithospheric structure, basin inversion and regional uplift during the Late Cretaceous.
- The key mechanism of this flat slab is dynamic suction due to long-lived prior subduction along the west Pacific and south Asian margins.

Abstract

The existence of historical flat slabs remains debated. We evaluate past subduction since 200 Ma using global models with data assimilation. By reproducing major Mesozoic slabs whose dip angles satisfy geological constraints, the model suggests a previously unrecognized continental-scale flat slab during the Late Cretaceous beneath East Asia, a result independent of plate reconstructions, continental lithospheric thickness, convergence rate, and seafloor age. Tests show that the pre-Cretaceous subduction history, both along the western Pacific and Tethyan trenches, is the most important reason for the formation of this prominent flat Izanagi slab. Physically, continuing subduction increases the gravitational torque, which, through balancing the suction torque, progressively reduces dynamic pressure above the slab and decreases the slab dip angle. The flat Izanagi slab explains the observed East Asian lithospheric thinning that led to the formation of the North-South Gravity Lineament, tectonic inversion of sedimentary basins, uplift of the Greater Xing'an-Taihang-Xuefeng mountains and the abrupt termination of intraplate volcanism during the Late Cretaceous.

1. Introduction

Different from normal subduction, flat slabs have small dip angles and lie nearly horizontally beneath an overriding plate. The best examples for ongoing flat subduction are those beneath South America, clearly seen in geophysical images (Gutscher et al., 2000; Hayes et al., 2012) and likely caused by subducting oceanic plateaus and nearby cratonic roots (Hu & Liu, 2016; Manea et al., 2012). However, due to sparse observational constraints, the existence and mechanisms of flat slabs during the geological past remain debated, especially in regions with a complex tectonic history. A notable example is the Late Cretaceous-Early Cenozoic Farallon flat slab beneath the western North America (Liu et al., 2010; Saleeby, 2003). This phase of flat subduction is confirmed from many aspects, including the Laramide orogeny (DeCelles, 2004; Fan & Carrapa, 2014; Saleeby, 2003), the migrating magmatic arc (Coney & Reynolds, 1977; Henderson et al., 1984; Liu et al., 2021), the widespread Cretaceous marine inundation (Bond, 1976; Heller & Liu, 2016; Chang & Liu, 2020), and confirmation from both forward and adjoint geodynamic modeling (English et al., 2003; Liu et al., 2008; Liu & Currie, 2016). Other examples include the Mesozoic flat subduction in East Asia (Li & Li, 2007; Liu et al., 2019; Wu et al., 2019;

Xu, 2001), although questions still remain on the temporal and spatial extents of these events as well as their mechanisms (Liu et al., 2021).

Although uncertainties exist about past flat subduction, several lines of consensus emerge from previous studies. Besides the above mentioned upper-plate behaviors, including orogenic uplift in the hinterland (e.g., Fan & Carrapa, 2014), migration or shutoff of magmatic arcs (e.g., Henderson et al., 1984; Liu, 2015), and contemporary inland subsidence (e.g., Dávila & Lithgow-Bertelloni, 2015; Heller & Liu, 2016), another growing agreement is that flat slab subduction could efficiently deform and thin the overriding continental lithosphere (Axen et al., 2018; Bird, 1988; Liu et al., in review). Indeed, all or some of these characteristics have been directing the search for past events of flat subduction, especially in regions with a complex tectonic history and imperfect mantle seismic images like East Asia (Li & Li, 2007; Wu et al., 2019).

The past decades of research also presented multiple potential mechanisms for the formation of flat slabs. These can be summarized in the following four categories. (1) Fast convergence rate, especially with the trench-ward movement of a thick overriding plate (van Hunen et al., 2000). This mechanism was used to explain both the Cretaceous western U.S. Laramide slab (Coney & Reynolds, 1977; Liu & Currie, 2016) and the Cenozoic South American flat slabs (Hu et al., 2016). (2) Increased slab buoyancy, including young seafloor ages and subduction of an oceanic plateau. This is exemplified by the Laramide-type flat slabs in the Americas (Gutscher et al., 2000; Liu et al., 2010) and East Asia (Li & Li, 2007; Wu et al., 2019). (3) Hydrodynamic suction force within the mantle wedge (Stevenson & Turner, 1977), which could be enhanced by an approaching cratonic root, with an example being the central Chillean flat slab (Hu et al., 2016; Manea et al., 2012). (4) Effects due to long-lasting prior subduction, a recently proposed mechanism based mostly on observing present-day subduction properties (Hu & Gurnis, 2020) and generic numerical models (Schellart, 2020). The physics and dynamics of this last mechanism still needs more work.

Carrying the above spirit of searching and understanding unknown flat subduction events, we reproduce the past subduction history on Earth since the early Mesozoic using a high-resolution global simulation, where we consider thermal-chemical convection (e.g., Hu et al., 2018b) that better represent realistic subduction processes than previous models that are always regional in scale and generic in nature (e.g., Huangfu et al., 2016; van Hunen et al., 2004; Schellart, 2020).

Our global subduction models are more Earth-like because they are also based on a sophisticated data-assimilation technique (Hu et al., 2016, 2018b; Liu & Stegman, 2011) such that the model inputs are consistent with recent plate reconstructions (e.g., Müller et al., 2016; Seton et al., 2012). Based on these models, we look for possible historical flat slabs. As shown later, the model properly reproduced Mesozoic past subduction along all major convergent boundaries, with the resulting slab dip angles consistent with geological constraints. Among these, both western North America and East Asia experienced a phase of continental-scale flat slab during the Late Cretaceous. The latter represents a previously unrecognized scenario of flat subduction that can explain multiple aspects of the enigmatic tectonic history of East Asia. We further demonstrate that formation of this flat slab results from a combination of multiple proposed mechanisms.

2. Methods and model setup

Previous geodynamic studies on flat slab subduction mostly utilized regional models with idealized initial and boundary conditions. To better understand global subduction since the early Mesozoic, especially the existence and mechanisms of flat slabs, we quantitatively reproduced subduction history during the past 200 Ma using 4D global thermal-chemical models with data assimilation (Hu et al., 2016; Hu et al., 2018b; Liu & Stegman, 2011). The numerical simulations are carried out with the spherical mantle code CitcomS (McNamara & Zhong, 2004; Tan et al., 2006; Zhong et al., 2008). The mantle is discretized into a high-resolution mesh with 12 spherical caps each having 257×257×113×12 nodes in latitude×longitude×radius. The lateral resolution is ~23 km at the surface that reduces to ~12 km at the core-mantle boundary (CMB). In the vertical direction, an uneven mesh is used with a ~12 km resolution near the surface, ~26 km near the CMB, and ~31 km in the mid-mantle.

2.1. Governing equations

We assume an incompressible mantle that satisfies the Boussinesq approximation. The equations for the conservation of mass, momentum and energy are:

$$\nabla \cdot \vec{u} = 0, \tag{1}$$

$$-\nabla P + \nabla \cdot [\eta(\nabla \vec{u} + \nabla^T \vec{u})] + (\rho_m \alpha \Delta T + \Delta \rho_c)\vec{g} = 0, \tag{2}$$

$$\frac{\partial T}{\partial t} + \vec{u} \cdot \nabla T = \kappa \nabla^2 T, \tag{3}$$

$$\frac{\partial C}{\partial t} + \vec{u} \cdot \nabla C = 0, \tag{4}$$

where $\vec{u}$ is the velocity, P is dynamic pressure, η is dynamic viscosity, ρ_m is the density of the ambient mantle, α is thermal expansion coefficient, ΔT is temperature anomaly, $\Delta\rho_c$ is compositional density anomaly, $\vec{g}$ is gravitational acceleration, and C is composition.

2.2. Boundary conditions

The base of the mantle is assumed to be free slip. The surface assimilates velocities based on recent plate reconstructions. To quantify the influence of surface boundary conditions on mantle dynamics and slab evolution, we adopted several different plate reconstruction models (Müller et al., 2016; Müller et al., 2019; Seton et al., 2012) into our global simulations and and compared their results. We also considered another recent reconstruction (Torsvik et al., 2019) for a comprehensive comparison of the Mesozoic kinematics in the western Pacific (Fig. S1).

The temperature profile for the oceanic plates follows a modified plate model (Hu et al., 2018b; Liu & Stegman, 2011) (Fig. S2a). This way, the temperature difference across the thermal boundary is reduced to ~700ºC from ~1300ºC, in order to better resolve the evolving slab dynamics while conserving energy with a finite resolution of a discretized mesh. The convection vigor in our models remains similar to that in studies with a larger temperature contrast (Ma et al., 2019; Mao & Zhong, 2018), but whose upper-mantle dynamics is compromised with either semi-vertical slabs or parameterized slab geometry and kinematics. The evolving seafloor age that determines oceanic plate's thermal profile is based on plate reconstructions (Müller et al., 2016; Müller et al., 2019; Seton et al., 2012).

The continental plates have an initial steady-state geotherm, whose structure subsequently evolves in response to subduction dynamics. The initial thickness of the continental lithosphere varies among models, for testing their effect on slab dynamics. The CMB temperature is fixed at 500ºC higher than the that of the ambient mantle. This is lower than that in some earlier studies (Hassan et al., 2016; Zhang & Li, 2018), but it has little effect on subduction dynamics, due to the relatively short model history and the existence of a dense compositional layer above the CMB that prohibits excessive plume formation.

2.3. Compositional structure

We considered the effects of third different chemical compositions to reproduce realistic mantle dynamics, where a total number of about 1.8 billion chemical tracers are used. The

continental lithosphere consists of a 2-layer crust and 3-layer mantle lithosphere. The average density of continental crust is about 2.8 g/cm^3 with the lower crust being weaker than the upper crust, in order to minimize the effect of imposed surface kinematics on lithospheric deformation at depth. The mantle lithosphere has a chemically buoyant upper layer, a neutrally buoyant middle layer and a dense lower layer, all relative to the ambient mantle, following a recent inference (Hu et al., 2018a). The overall buoyancy of the continental mantle lithosphere is similar to that of a purely thermal mantle lithosphere, such that the resulting continental topography resembles that observed.

The oceanic plate is approximated with three different compositions: a weak surface layer, a basaltic crustal layer and the underlying lithospheric mantle. The top 7-km of thickness mimics the viscosity effect of a weak and lubricating plate interface upon subduction. Further below, we define a 21-km thick (due to the limited vertical resolution) crustal layer whose total buoyancy is the same as that for a 7-km thick oceanic crust with a density of 3.0 g/cm^3. When the chemically buoyant oceanic crust subducted to 120 km or deeper, its composition and density change following the basalt-to-eclogite phase transformation.

At the base of the mantle, we also define an initial 250-km thick chemical layer whose compositional density anomaly is about +2.4%. This layer evolves in response to subducting slabs and its internal thermal structure, that also generates hot plumes from time to time. By solving both thermal and compositional evolution of the mantle, our models are more capable to reproduce the multiple-scale slab dynamics, especially at shallow mantle depths, compare to the pure-thermal simulations commonly used in earlier studies.

2.4. Viscosity structure

The models incorporate a 3D viscosity structure that depends on depth, temperature and composition (Fig. S2b), following

$$\eta = \eta_0 \cdot C \cdot exp\left(\frac{E_\eta}{T+T_\eta} - \frac{E_\eta}{T_m+T_\eta}\right), \quad (5)$$

where η is the effective viscosity, η_0 is the background viscosity (Fig. S2b), C is the compositional multiplier, E_η is the activation energy, T_η is the activation temperature, T is temperature and T_m is the background temperature. The reference viscosity is 10^{21} Pa·s, and the resulting lateral viscosity variation is up to 4 orders of magnitude. We choose the values of other

physical parameters to best match the present-day seismic image for subducted slabs. More details about the model setup and subduction simulation are in Hu et al. (2018b).

3. Results

Due to the many sophisticated model features, both in composition and viscosity, these global thermal-chemical models are very expensive to achieve. For a standard case, one full simulation starting from 200 Ma takes ~300,000 core-hours to finish. On the other hand, these simulations also better present the real Earth in that the resolved subducting slabs are strictly one-sided with sharp viscosity and density variations across the subduction zone. More importantly, the modeled slabs could readily deflect and deform in response to lateral mantle dynamics, such as pressure gradients and mantle flow. Consequently, we observe a rich history of slab evolution and morphology, ranging from normal to flat subduction, and from continuous to segmented slabs. As shown later, thus reproduced subduction history largely matches those observed/inferred along major subduction zones around the globe since the early Mesozoic. Another important outcome of these models is the temporal variation of the overriding plate, especially in the case of continental lithosphere. These allow a wide-range comparison of model results with geophysical and geologic data constraints.

We present a total of eleven global models, with a focus on slab evolution under different tectonic conditions. Model 1 is the reference case, which is fully analyzed in this study. This model assimilates the surface velocity and seafloor age from Müller et al. (2016), and runs from 200 Ma to the present. The initial continental lithospheric thickness is 160 km. Models 2 and 3 have the same setting as Model 1 except that the surface boundary conditions are constrained by Seton et al. (2012) and Müller et al. (2019), respectively. Models 4 and 5 are used to test the effect of the continental lithospheric thickness, which is 200 km and 120 km, respectively. Models 6-8 differ from Model 1 in that: Model 6 starts from 160 Ma (to test the effect of trench migration), Model 7 has a maximum subduction rate of 12 cm/yr after 120 Ma (to test the effect of subduction rate), Model 8 has a uniform sea floor age of 50 Myrs old after 120 Ma (to test the effect of seafloor age). Models 9-11 are to test the effect of duration of continuous subduction, with the starting age being 120, 100 and 80 Ma, respectively.

3.1. Simulated global subduction since the middle Mesozoic

In an earlier attempt to reproduce past global subduction (Hu et al., 2018b), we show that the predicted present-day slab geometry and location below major subduction zones closely match those from seismic tomography. The new model (Model 1) presented here has a further improved fit to tomography, especially in regions with uncertain Mesozoic plate kinematics, such as East Asia. Consequently, the fit to the present mantle structures lends credibility to the simulated past subduction (Fig. 1).

Since 200 Ma, subduction along major trenches (North America, South America, East Asia and South Asia) has been predominantly normal, with a >30º dip angle in general, with brief fluctuations of slab dip angle resulting in steep to shallow dipping subduction. For example, the predicted overall normal slab dip angles during the Mesozoic along the South American and Tethyan trenches are consistent with the locations of their respective volcanic arcs during this history (Kapp & Decelles, 2019; Trumbull et al., 2006). Next, we will focus on the continental-scale behavior of slab dip variations, especially flat subduction (e.g., Fig. 1).

During the entire model history, we observe the occurrence of two prominent (extending no less than 1000 km inland) flat slabs, both at a continental scale (>1000 km wide along trench), long lasting (for 40-50 Myrs), and occurring in the Late Cretaceous to Early Cenozoic. One is the well-studied Farallon flat slab from 90 to 40 Ma within the western North America (Figs. 1, S3). The modeled flat Farallon slab reached an inland distance of ~1000 km at the maximum, consistent with but slightly shorter than inferences from structural deformation (Saleeby, 2003) and that in time-reversed convection models based on tomography images (Liu et al., 2008; Liu et al., 2010). Formation of the flat Farallon slab has been commonly attributed to the fast motion of the overriding plate (e.g., van Hunen et al., 2000; Liu & Currie, 2016). Consideration of a buoyant oceanic plateau (Liu et al., 2010), a process not modeled here, may further increase the width of the flat slab. The reproduction of the Laramide flat slab in Model 1 confirms its improved capability for resolving past subduction over similar previous studies.

The other prominent flat slab occurred within the western Pacific, where the subducting Izanagi slab broadly underplated East Asia during the Late Cretaceous (100-60 Ma). The landward extent (up to 1600 km) of the flat Izanagi slab was even larger than that of the flat Farallon slab (Fig. 1). This flat slab was neither previously recognized nor reproduced in any earlier geodynamic models. An important way to constrain past subduction is to compare with the present-day mantle

structure (Hu et al., 2018b; Liu & Stegman, 2011). Figure 2 shows this comparison with seismic tomography MIT-P08 (Li et al., 2008). The Mesozoic slabs are predominantly within the lower mantle at the present, where both predicted geometry and location of the lower-mantle slabs match those revealed in tomography, providing an additional support for the modeled Mesozoic subduction within the western Pacific.

Another inference of late-Mesozoic flat subduction directly comes from the seismic image itself. The majority of the lower mantle slabs is located far west to the present-day trench, with a distance of up to 3000 km (Fig. 2c,d). However, the Eurasian Plate has experienced limited eastward translation (<1000 km) since the Mesozoic (Fig. S1), as demonstrated in several recent plate reconstructions (Müller et al., 2016; Müller et al., 2019; Seton et al., 2012; Torsvik et al., 2019). This large east-west offset between the Mesozoic slab and present-day trench location suggests a significant horizontal displacement of the slab during the past. From the evolution of different major slabs (Fig. S3), a broad Mesozoic flat slab provides a natural explanation for the present-day seismic image. This reasoning is effectively the same as the inference of the flat Farallon slab during the Late Cretaceous (Figs. 1, S3) based on geodynamic modeling using seismic images (Bunge & Grand, 2000; Liu et al., 2008).

3.2. Geological constraints on a potential Late-Cretaceous flat Izanagi slab

Here we further evaluate the predicted Late-Cretaceous flat Izanagi slab following the common exercises on constraining the flat Farallon slab (Axen et al., 2018; Liu et al., 2010; Saleeby, 2003). We first emphasize that, due to the poorly known Mesozoic subduction history in the western Pacific, our model result represents a previously unrecognized episode of flat slab that could have significantly affected the tectonics of the region. However, before a final conclusion is achieved, multiple additional aspects of the model and surface geology need to be examined, similar to that done for the Farallon flat slab mentioned above.

Since there are considerable amounts of uncertainty in the Mesozoic plate motion (Fig. S1), we further tested models (Model 2 and Model 3) constrained by two other plate reconstructions (Müller et al., 2019; Seton et al., 2012). These reconstructions show quite different histories of west Pacific subduction and East Asian motion from that use in Model 1 (Fig. S1). Although the resulting Late-Cretaceous slab geometries from Models 2 & 3 are not identical to that in Model 1, both these models also clearly demonstrate a flab Izanagi slab (Fig.

S4) whose location and timing are largely consistent with that in the reference case. Thus, we conclude that the Late-Cretaceous East Asian flat slab represents a robust model result that is independent of surface kinematic conditions.

Next, we focus on evaluating the flat Izanagi subduction with several unique aspects of the Mesozoic tectonic history of East Asia, including the enigmatic formation of the North-South Gravity Lineament (NSGL), the abrupt inversion of major sedimentary basins east of the NSGL, and the synchronous exhumation of the NSGL-parallel Greater Xing'an-Taihang-Xuefeng mountains. Refer to a detailed review of the region's Mesozoic tectonic history and possible links to past flat subduction events (Liu et al., in review).

First, the NSGL highlights strong east-west contrasts in topography (Fig. 3a), Bouguer gravity anomaly (Xu, 2007), crustal thickness (Li et al., 2014) and lithospheric thickness (Fig. 3b). It cuts through major east-west trending Early-Mesozoic tectonic belts (Yinshan-Yanshan Orogen, Qinling-Dabie Orogen and Jiangnan Orogen) in East Asia (Fig. 3a). This implies that the appearance of the NSGL is likely after the formation of these east-west tectonic belts. This provides a first-order age constraint for the formation of the NSGL to be no earlier than the Cretaceous (Xu, 2007). Previous studies show that a flat slab can result in thinning of the overriding continental lithosphere, with the amount of thinning depending on the model setup (Axen et al., 2018; Bird, 1988). Multiple conceptual models of East Asian flat subduction were proposed (Li & Li, 2007; Liu et al., 2019; Wu et al., 2019; Zhang et al., 2010), but they all imply more restricted spatial extents and at earlier times relative to those of the NSGL.

In contrast, the flat Izanagi slab in our model underplated the entire N-S range of East Asia (Fig. 4). During its development, the western edge of the flat slab advanced westward until it reached the location of the NSGL by 70 Ma when the flat slab reached the maximum inland extent (Fig. 4). This flat slab had an east-west length of ~1600 km in South China (e.g., 32ºN) and of ~1800 km in North China (e.g., 43ºN). With the development of the flat slab, the overriding Eurasian mantle lithosphere was eroded by the slab (Fig. 4c-e), leading to a much reduced lithospheric thickness to the east of the NSGL. In addition, some eroded and displaced continental lithospheric material accumulated at the western end of the flab slab to form a deep root. This lithospheric root is also consistent with several seismic studies (Chen et al., 2014; Liu

et al., 2004; Sun & Kennett, 2017). These observations suggest that lithosphere thinning due to the newly revealed flat slab is a plausible mechanism for the formation of the NSGL.

During flat slab subduction, the overriding plate tends to experience lithospheric compression, as seen in the typical Laramide Orogeny (DeCelles, 2004; Liu et al., 2010). In East Asia, almost all major sedimentary east of the NSGL (e.g., Songliao Basin, Bohai Bay Basin and Hefei Basin in Fig. 3 insert figure) experienced a ~30-Myr period of inversion during the Late Cretaceous (Liu et al., 2017; Liu et al., 2020). Origin of this continental-scale basin inversion remains elusive, where previous proposals including changing plate motion and/or trench advance around this time (Liu et al., 2017; Song et al., 2014), both suggestions not supported by recent plate reconstructions (e.g., Fig. S1). Our model, on the other hand, suggests that the flat slab provides a direct mechanism for this event. Indeed, the transition from extensional/strike-slip type of stress at 120 Ma (Fig. S5a) to strong east-west compressional stress at 70 Ma (Fig. S5b) within East Asia is consistent with the change from rapid Early-Cretaceous deposition to regional-scale Late-Cretaceous basin inversion. During this process, the flat subduction induced compression thickened the buoyant upper mantle lithosphere (Fig. 4c-d), and likely thickened the crust as well, the latter not simulated here due to imposed surface kinematics. Consequently, the resulting surface uplift caused the basin inversion.

Another important indication for surface uplift is orogenic exhumation (e.g., Fan & Carrapa, 2014). While the time for the formation of the NSGL is constrained to be Late Mesozoic, Xu (2007) further used the time of Taihang Mountain uplift to suggest that the NSGL formed in Early Cretaceous. In this study we revisited the cooling history of the Greater Xing'an-Taihang-Xuefeng mountain chain that is goes along the NSGL. According to recent thermochronology studies (Clinkscales et al., 2020; Ge et al., 2016; Pang et al., 2020; Qing et al., 2008), all these mountains experienced rapid cooling during the Late Cretaceous (Fig. 3c). These cooling events were previously attributed to different mechanisms, including orogenic uplifts (Ge et al., 2016; Pang et al., 2020; Qing et al., 2008) and extension (Clinkscales et al., 2020). Given that both the timing and spatial distribution of the flat slab in our model (Fig. 4) match those of the basin inversion and orogenic exhumation (Fig. 1), we suggest the regional compression and uplift due to flat subduction provides an ultimate mechanism to these surface records. Formation of the deep lithospheric roots right below the Greater Xing'an-Taihang-Xuefeng mountains (Fig. 4e) also seems to suggest a causal relationship.

Based on the strong consistency between the modeled flat Izanagi slab and various tectonic observations, we suggest that uplift of the Greater Xing'an-Taihang-Xuefeng mountains and thinning of the lithosphere to the east characterize the formation of the NSGL during the Late Cretaceous.

3.3. Evaluating proposed mechanisms for slab flattening

While a Late-Cretaceous flat Izanagi slab was consistently produced in models assimilating constraints from different plate reconstructions, the mechanism for the observed slab flattening still remains to be investigated. Here we will evaluate all previously proposed mechanisms including (1) enhanced hydrodynamic suction, (2) large convergence rate, (3) increased slab buoyancy, and (4) long-existing prior subduction. The first mechanism mainly concerns the effect of a thick cratonic overriding plate that helps to increase the suction force and reduce to slab dip (Hu et al., 2016; Jones, 2012; Liu & Currie, 2016; Manea et al., 2012). In Model 1, all continents have the same initial thickness (160 km), with no thick cratonic roots included. As shown above (Figs. 4, S3), flat subduction in East Asia did not appear within the first 100-Myr of model time, and the Late-Cretaceous slab flattening was not assisted by any nearby thick craton. Therefore, increased suction due to thick overriding cratonic plate is not the reason for the flat Izanagi slab. We further run Model 4 and Model 5, with overriding plate lithospheric thickness being 200 km and 120 km, respectively. The observation that both these two models result in a similar flab Izanagi slab confirms that the lithospheric thickness of the overriding plate is not important for the formation of flat subduction (Fig. 5a-c).

The convergence rate is the sum of the overriding plate motion (equal to trench migration rate if neglecting intraplate deformation) and subducting plate motion. To test the potential effect of trench motion prior to the formation of the flat slab, we performed another model (Model 6), which started from 160 Ma instead of 200 Ma. Since the net trench migration during 160-60 Ma is very small ($<10^{o}$ arc length, Fig. S1), this model also represents a scenario where the long-term trench effect is negligible. Surprisingly, Model 6 also generated a flat Izanagi slab (Fig. 5d) with almost identical geometry to that in Model 1 (Fig. 5a). Based on these model results (Fig. 5a,d), we confirm that trench migration is not the reason for the formation of the Late-Cretaceous flat Izanagi slab.

Another key component of the convergence rate is the speed of the subducting plate. Recent plate reconstructions suggest that the subduction speed of the Izanagi plate increased significantly during the Late Cretaceous (Müller et al., 2016; Müller et al., 2019; Seton et al., 2012). According to Müller et al. (2016), the average Izanagi plate velocity during 120-100 Ma is about 12 cm/yr (Fig. S6). After that the Izanagi plate sped up, with the velocity going up to 23 cm/yr by 80 Ma. The fast subduction speed was also proposed as a possible reason for the Late-Cretaceous flat subduction of the Farallon plate (Coney & Reynolds, 1977). Since the modeled slab became flattened after ~100 Ma (Fig. S3), which corresponds to the time of Izanagi speeding up (Fig. S6), we performed another model (Model 7), in which the upper limit of the subduction speed is capped at 12 cm/yr after 120 Ma but other model setup remains the same as that in the reference model. However, we observe that without the period of fast Izanagi plate motion, the flat Izanagi slab still came into being during the Late Cretaceous, where the resulting slab geometry (Fig. 5e) is almost identical to that in the reference case (Fig. 5a). This additional model result suggests that the fast subduction speed is not causing the predicted flat slab. Collectively, the results from these cross sections (Fig. 5a,d,e) imply that the convergence rate is not the reason for the formation of the flat Izanagi subduction.

Increased slab buoyancy force is another popular mechanism to explain the origin of flat subduction (van Hunen et al., 2002; Liu et al., 2010). Common approaches for increasing slab buoyancy include the presence of oceanic plateaus within the ambient seafloor and the presence of young seafloor age. In our models, the thermal structure of the oceanic lithosphere follows the plate model, where the lithospheric thickness varies when seafloor age is less than 80 Myrs. However, no oceanic plateau is included within the Izanagi plate for any time during the simulation. This proves that an oceanic plateau is not required for the occurrence of the flat subduction. Regarding the effect of young seafloor age, a consensus based on multiple plate reconstructions (Müller et al., 2016; Müller et al., 2019; Seton et al., 2012) is that the Izanagi plate became younger at the trench during the Late Cretaceous, prior to the Izanagi-Pacific mid-ocean ridge entering the subduction zone at around 55 Ma. Thus, the slab age could be as young as 10 Ma during the latest Cretaceous. Since the average seafloor age of the Izanagi Plate during the Late Cretaceous is about 50 Myrs, we designed a new model (Model 8) whose seafloor age remained as 50 Myr-old after 120 Ma. Model 8 is otherwise the same as the reference model. Interestingly, this model still reproduced the Late-Cretaceous flat slab (Fig. 5f). Although minor

differences in slab thickness and geometry exist in this simulation, the length of the resulting flat slab is very similar to that in Model 1 (Fig. 5a). Based on these results, we conclude that the slab age is not a dominant control on the generation of the flat Izanagi slab as well.

3.4. The role of former subducted slabs

Active subduction will generate low (high) dynamic pressure above (below) the slab (Stevenson & Turner, 1977). The resulting pressure-gradient across the slab, also called hydrodynamic suction, is balanced by the negative buoyancy of the slab to maintain a certain dip angle. Consequently, a larger pressure-gradient results in a smaller slab dip (Stevenson & Turner, 1977). This dynamic relationship is commonly observed in our model. Take the reference model for an example (Fig. 6), at 160 Ma (40 Myrs after subduction initiated), the dynamic pressure in the mantle wedge was only slightly lower than that below the slab hinge, as correlated with a relative steep Izanagi slab (Fig. 6a). By 120 Ma (80 Myrs of continuous subduction), the low pressure within the mantle wedge became more prominent, and meanwhile the slab dip was also notably reduced (Fig. 6b). This trend progressed further into the Late Cretaceous, during which the slab became progressively flatter while the dynamic pressure above the slab continued to decrease (Fig. 6c,d). A similar evolution history of dynamic pressure and slab dip also occurred along the Tethyan subduction zone in South Asia (Figs. 6, S3).

While the above corner-flow analysis explains the instantaneous force balance of an evolving subducting slab, it remains unclear what drives the progressive pressure reduction above the slab and the reduction in slab dip during the late Mesozoic. With more tests, we found that the duration of continuous prior subduction along the same trench is the key reason for the observed slab flattening. To illustrate this causal relationship, we compared the model results (i.e., dynamic pressure and slab geometry) at 70 Ma from four models that have different starting ages of subduction (Fig. 7): 200 Ma (Model 1), 160 Ma (Model 6), 120 Ma (Model 9), 100 Ma (Model 10) and 80 Ma (Model 11), respectively. Overall, with an earlier starting age, the resulting Late-Cretaceous slab dip is smaller (Figs. 7, S7, S8). When subduction started at 80 Ma, the slab by 70 Ma was steeply subducting and barely reached the base of the upper mantle (Figs. 7e, S7e). As the starting age increases to 100 Ma, the slab at 70 Ma was more shallowly dipping but not flattened, with its lower end entering the lower mantle (Figs. 7d, S7d). An upper-mantle flat-slab started to form at 70 Ma as we push the starting age back to 120 Ma (Figs. 7c,

S7c). In this case (Model 9), the length of the flat slab is notably smaller than that in Model 1 (Fig. 7a). This relationship is further confirmed with Model 6 whose subduction started at 160 Ma (Fig. 7b), where the length of the 70-Ma flat slab is almost identical to that in Model 1 (Fig. 7a). Another way to understand the above statement is through analyzing the mean slab dip angle at different depth ranges (Fig. 7f). The shallow portions of the slab (0-300 km) demonstrate a clear trend with the dip angle decreasing as the subduction duration increases. This finding suggests that the deep mantle dynamics associated with different subduction durations strongly controls the slab dip above 300 km depth, where the resulting dynamic pressure plays a dominant role. The actively descending slabs, regardless of their depths, are affecting the upper mantle dynamic pressure distribution and thus the slab dip at shallow depth. According to Wu et al. (2019), the Late-Jurassic flat slab below North China started to steepen after 160 Ma, a process not modeled here. The fact that Model 1 and 6 have similar results (Figs. 7a,b, S8a,b) demonstrates that subduction prior to 160 Ma has little effect on the formation of the 70-Ma flat slab. Therefore, the Late-Cretaceous flat slab represents an independent result from subduction prior to the Cretaceous.

Importantly, these models reveal that the dynamic pressure above the 70-Ma slab became progressively more negative as the initial subduction occurred earlier (Fig. 7). This suggests that a longer subduction history, thus a greater length of the downgoing slab, exerts a stronger downward pull and exacerbate depressurization of the mantle above the slab. Consequently, this leads to a greater dynamic pressure-gradient across the slab, which, by preferentially affecting the upper-mantle portion of the slab, causes continuous reduction in the slab dip angle over time. A more quantitative analysis of this mechanical process is presented later in the discussion part. This reasoning is also consistent with the steady increase of pressure-gradient across the slab and temporal decrease of slab dip angle during the Cretaceous in the reference model (Fig. 6). Mechanically, the scenarios in Figure 6a,b are similar to the proposed shallowing of the South American slab from the Cretaceous to the Cenozoic (Schellart, 2017). Furthermore, our study explains the recent finding that the subduction duration negatively correlates with the slab dip angle observed at the present day (Hu & Gurnis, 2020) and is consistent with a recent regional study (Schellart, 2020).

Regarding the formation of the Late-Cretaceous flat Izanagi slab, nearby subduction may also have played a role. Besides the western Pacific, another major subduction zone, the Tethyan

trench along South Asia, has been active since the early Mesozoic (Müller et al., 2016). Although the Tethyan subducting slab was more segmented than the Izanagi slab due to intervening terrane accretion, a broad low-pressure mantle region above the Tethyan slab formed prior to that above the Izanagi slab (Fig. 6a), and the pressure also became progressively more negative over time (Fig. 6b-d). The Tethyan low-pressure zone expanded to merge with that along East Asia by ~140 Ma and excited notable westward flow beneath East Asia throughout the deep mantle since then (Figs. 6, S3). We suggest that this augmented hydrodynamic suction force across the East Asian subduction system further facilitated the ultimate flattening of the Izanagi slab during the Late Cretaceous (Fig. 6).

An examination of global subduction suggests that most of the normal slab dip scenarios were associated with intermittent subduction or when the continuous slab length was small. For example, in South Asia and South America, the slabs were generally short with intermittent subduction periods, and the dip angles were large (Figs. 1, S3). For South America, the shallow slab dip angle decreased during the Cenozoic because of the continuous subduction (Fig. S3). These are in contrast to the Izanagi slab (at 70 Ma) and the Farallon slab (at 40 Ma) that evolved into long, continental scale flat slabs, before which both regions had a continuous subduction duration of 130 Myr (Figs. 1, S3). Besides previous mechanisms for the flat Farallon slab such as oceanic plateau subduction (Liu et al., 2010) and fast overriding plate motion (Liu & Currie, 2016), this study suggests that the long subduction duration may have also contributed to the flattening of the Farallon slab. These global slab behaviors further support our new mechanism that long prior subduction duration is important for flat subduction to occur, with a newly identified widespread flat slab below the Late Cretaceous East Asia (Figs. 1, 4).

3.5. Physical mechanism for the flat Izanagi slab

To further understand the physical mechanism, we will take a closer look at the suction torque and gravity torque whose balance determines the slab dip angle. As shown above, the slab dip at shallow mantle depth strongly depends on subduction duration. This mechanism could be more quantitatively explained through the evolving force and torque balance between dynamic pressure and slab dip angle. For simplicity, we assume a stationary trench, where the slab subducts at velocity U, with a depth-invariant dip angle θ over a slab length L (Fig. 8a). According to Stevenson and Turner (1977), the dynamic pressure at a given depth in the sub-slab

region A is higher than that in the mantle wedge B, forming a pressure gradient across the slab, whose magnitude is positively correlated with *U*, negatively with θ, but independent of *L*. This pressure difference, when integrated along the slab length *L*, leads to a hydrodynamic suction torque (per unit trench length) defined around the trench:

$$T_H = 2\eta UL\left[\frac{\sin\theta}{(\pi-\theta)+\sin\theta} + \frac{\sin^2\theta}{\theta^2-\sin^2\theta}\right]. \quad (6)$$

This torque tends to rotate the slab to reduce its dip θ. On the other hand, the gravity force due to negative buoyancy of the slab exerts an opposite-sensed torque

$$T_G = \frac{1}{2}bL^2\cos\theta, \quad (7)$$

where *b* is the average negative buoyancy per unit slab area. The balance between T_H and T_G determine the slab dip θ, as shown in Figure 8b.

To understand the effect of slab length *L* on slab dip θ, we first define a reference scenario of torque balance: for a given value of *L*, there exists a value of b that satisfies $T_H = T_G$; this corresponds to a critical slab buoyancy $b_c \approx 20\eta U/L$ and to a critical dip angle $\theta_c \approx 63°$ (Stevenson & Turner, 1977). While the suction term ($T_H/2\eta UL$) in Figure 8 only depends on θ, the gravitational term is affected by more factors, including mantle viscosity (η), subduction rate (*U)*, slab length (*L)*, slab thickness and density. For convenience, we use the ratio $r_b = b/b_c$ to evaluate the torque balance. Assuming that mantle viscosity, subduction rate, slab thickness and density are constants during subduction, the ratio r_b will depend only on slab length *L*. As *L* increases, *b* becomes larger than b_c, which will result in two balancing points, one with a smaller dip angle and the other with a larger dip angle. These two balancing points will move progressively away from θ_c as *L* keeps increasing, with the slab eventually becoming flat ($\theta = 0°$) or vertical ($\theta = 90°$).

We suggest that the latter case (θ evolves toward 90° as *L* increases) is unlikely for East Asian subduction. For this scenario to occur, the initial slab dip needs to reach the critical value of 63°. Here this initial condition should be a scenario when *L* is significantly larger than the slab thickness, in order to satisfy the thin-slab assumption (Stevenson & Turner, 1977). As recent studies demonstrate, the slab is relatively steep before its downdip end gets anchored in the high-viscosity lower mantle (e.g., Schellart, 2017), and the depth-averaged slab dip in this case

usually stays significantly lower than 60° (Hu & Gurnis, 2020). For East Asia, the dip angle was large prior to 160 Ma due to the fast trench advance (Fig. S1). However, after that the slab dip angle slowly decreased. From 140 to 120 Ma, the average upper-mantle slab dip kept less than 45° (e.g., Fig. S3). Consequently, the subsequent torque balance as subduction continues will evolve toward lowering instead of increasing the slab dip (Fig. 8b). It is notable that this torque balance promotes a positive feedback between the reducing slab dip and dynamic suction (Fig. 8b), which facilitates the eventual formation of a flat slab (Figs. 6, S3). In reality, slabs are not infinitely rigid as assumed here. Therefore, the increasing suction torque with growing L will cause the slab to internally bend, a process that should follow the local dynamic pressure gradient. The observed increasing pressure gradient with decreasing depth (Figs. 6, 7) means that the shallowest slab is most susceptible to flattening (Fig. S3). This is also consistent with the finding that the slab above 300 km depth demonstrates the strongest dependence on the accumulating dynamic pressure over time (Fig. 7).

Consequently, the mechanism for this newly discovered Late-Cretaceous Izanagi flat slab represents a combination of two existing hypotheses: the long-existing prior subduction gradually builds up the hydrodynamic suction force within the mantle wedge that eventually leads to the continental-scale flat slab beneath East Asia. Therefore, both our discovery of the flat East Asian slab and its physical mechanism present new knowledge to the field of geodynamics and tectonics.

4. Discussion and conclusion

In this study, we investigated the Mesozoic subduction of the western Pacific with global data-assimilation models. A robust model result is the flattening of the Izanagi slab during the Late Cretaceous as long as western Pacific subduction started prior to the Cretaceous, a finding largely independent of the chosen plate reconstruction, continental lithospheric thickness, convergence rate and seafloor age evolution. More tests suggest that the former slabs generated along the same and nearby subduction zones are the key reason for the formation of this flat slab. The flat Izanagi slab during the Late Cretaceous represents a previously unrecognized subduction scenario.

The lithospheric thinning to form the NSGL, the inversion of eastern China sedimentary basins and the uplift of Greater Xing'an-Taihang-Xuefeng mountains may have all resulted from

the flab subduction. These geological implications are supported by some previous studies which revealed that flat subduction could cause orogenic uplift (Espurt et al., 2008; Liu et al., 2010) and lithospheric thinning (Axen et al., 2018; Bird, 1988). There are also other proposed mechanisms for the formation of the NSGL, among which the stagnant slab is a popular one (e.g., Liu et al., 2019; Xu, 2007). Recent modeling studies show that the presently observed stagnant slab did not form until the late Miocene, too late compared to the major tectonic events (Fig. 1). The flat Izanagi slab provides an alternative mechanism, as summarized in Figure 9, where the flat slab, thinned lithosphere and low present-day elevation east of the NSGL strongly correlate with each other.

Another common surface response during flat slab subduction is abnormal arc magmatism (Gutscher et al., 2000; Henderson et al., 1984; Liu et al., 2021). Within East Asia, widespread intraplate volcanisms, much of which had an arc affinity, sustained since the middle Mesozoic. These volcanisms rapidly waned during the Late Cretaceous and disappeared throughout most of East Asia by 80 Ma (Li, 2000; Liu et al., 2021; Liu et al., 2020; Tang et al., 2018; Zhou & Li, 2000). A definitive mechanism for this continental-scale magmatic shutdown is still lacking. Based on the match with many other independent Late-Cretaceous tectonic events, we suggest that our flat slab model provides an intuitive solution: During the period of flat subduction, the replacement of the former hot mantle wedge by the cold flat oceanic slab shut down preexisting volcanisms, forming a widespread and long-lasting magmatic lull.

Besides the balance of gravity torque and pressure torque as discussed before, there are other factors that may effect the slab dip angle as well, including a global scale eastward mantle flow (Doglioni, 1990) and toroidal flow around slab edges (Schellart et al., 2007; Liu & Stegman, 2011). However, a global scale west to east mantle flow tends to increase the dip angle of the Izanagi slab, opposite to the westward flattening of the slab that represents a robust result in this study. Thus, we suggest such an eastward global mantle flow should not exist. The toroidal flow, on the other hand, mainly affects the dip angel near the edges of the slab. For a wide subduction zone like in this study, the width of the trench is enormous and the region we focused on is far away from all the edges (Fig. 1). So, the toroidal flow should not play an important role in the flat Izanagi subduction as well.

For the case of East Asia, there are other relevant factors leading to the flat Izanagi slab. First, the subduction speed of Izanagi had been large during the late Mesozoic (Fig. S6). This could help maintain a relatively strong pressure gradient across the slab, facilitating slab flattening. Second, the adjacent Tethyan subduction could enhance the process of depressurization of the East Asian mantle. This became especially relevant as both the Izanagi and Tethyan slabs reach the deep mantle, when the strong slabs enclosed the East Asian mantle to build up the low-pressure region above the downgoing slabs (Fig. 6). In our model, the Tethyan and Izanagi slabs met each other to close up the mantle above them at about 100 Ma. This is also when the Izanagi slab started to flatten. A recent study implied that the Tethyan slab had a shallow slab dip during 85-65 Ma (Zhang et al., 2019a), a process also reproduced in our model (Fig. 1). This time also closely correlates with the peak stage of the flat Izanagi slab during 80-60 Ma (Fig. 4), supporting the mutual influence of the two giant subduction systems.

References

Axen, G. J., van Wijk, J. W., & Currie, C. A. (2018). Basal continental mantle lithosphere displaced by flat-slab subduction. *Nature Geoscience*, *11*(12), 961–964. https://doi.org/10.1038/s41561-018-0263-9

Bird, P. (1988). Formation of the Rocky Mountains, Western United States: A Continuum Computer Model. *Science*, *239*(4847), 1501–1507. https://doi.org/10.1126/science.239.4847.1501

Bunge, H., & Grand, S. P. (2000). Mesozoic plate-motion history below the northeast Pacific Ocean from seismic images of the subducted Farallon slab. *Nature*, *405*(6784), 337–340. https://doi.org/10.1038/35012586

Chen, L., Jiang, M., Yang, J., Wei, Z., Liu, C., & Ling, Y. (2014). Presence of an intralithospheric discontinuity in the central and western North China Craton: Implications for destruction of the craton. *Geology*, *42*(3), 223–226. https://doi.org/10.1130/G35010.1

Clinkscales, C., Kapp, P., & Wang, H. (2020). Exhumation history of the north-central Shanxi Rift, North China, revealed by low-temperature thermochronology. *Earth and Planetary Science Letters*, *536*, 116146. https://doi.org/10.1016/j.epsl.2020.116146

Coney, P. J., & Reynolds, S. J. (1977). Cordilleran Benioff zones. *Nature*, *270*(5636), 403–406. https://doi.org/10.1038/270403a0

578 Dávila, F. M., & Lithgow-Bertelloni, C. (2015). Dynamic uplift during slab flattening. *Earth and*
579 *Planetary Science Letters*, *425*, 34–43. https://doi.org/10.1016/j.epsl.2015.05.026
580 DeCelles, P. G. (2004). Late Jurassic to Eocene evolution of the Cordilleran thrust belt and
581 foreland basin system, western U.S.A. *American Journal of Science*, *304*(2), 105–168.
582 https://doi.org/10.2475/ajs.304.2.105
583 Doglioni, C. (1990). The global tectonic pattern. *Journal of Geodynamics*, *12*(1), 21–38.
584 https://doi.org/10.1016/0264-3707(90)90022-M
585 English, J. M., Johnston, S. T., & Wang, K. (2003). Thermal modelling of the Laramide orogeny:
586 Testing the flat-slab subduction hypothesis. *Earth and Planetary Science Letters*, *214*(3–4),
587 619–632. https://doi.org/10.1016/S0012-821X(03)00399-6
588 Espurt, N., Funiciello, F., Martinod, J., Guillaume, B., Regard, V., Faccenna, C., & Brusset, S.
589 (2008). Flat subduction dynamics and deformation of the South American plate: Insights
590 from analog modeling. *Tectonics*, *27*(3), 1–19. https://doi.org/10.1029/2007TC002175
591 Fan, M., & Carrapa, B. (2014). Late Cretaceous-early Eocene Laramide uplift, exhumation, and
592 basin subsidence in Wyoming: Crustal responses to flat slab subduction. *Tectonics*, *33*(4),
593 509–529. https://doi.org/10.1002/2012TC003221
594 Ge, X., Shen, C., Selby, D., Deng, D., & Mei, L. (2016). Apatite fission-track and Re-Os
595 geochronology of the xuefeng uplift, China: Temporal implications for dry gas associated
596 hydrocarbon systems. *Geology*, *44*(6), 491–494. https://doi.org/10.1130/G37666.1
597 Gutscher, M.-A., Spakman, W., Bijwaard, H., & Engdahl, E. R. (2000). Geodynamics of flat
598 subduction: Seismicity and tomographic constraints from the Andean margin. *Tectonics*,
599 *19*(5), 814–833. https://doi.org/10.1029/1999TC001152
600 Hassan, R., Müller, R. D., Gurnis, M., Williams, S. E., & Flament, N. (2016). A rapid burst in
601 hotspot motion through the interaction of tectonics and deep mantle flow. *Nature*,
602 *533*(7602), 239–242. https://doi.org/10.1038/nature17422
603 Hayes, G. P., Wald, D. J., & Johnson, R. L. (2012). Slab1.0: A three-dimensional model of
604 global subduction zone geometries. *Journal of Geophysical Research: Solid Earth*, *117*(1),
605 1–15. https://doi.org/10.1029/2011JB008524
606 Heller, P. L., & Liu, L. (2016). Dynamic topography and vertical motion of the U.S. Rocky
607 Mountain region prior to and during the Laramide orogeny. *Geological Society of America*
608 *Bulletin*, *128*(5–6), 973–988. https://doi.org/10.1130/B31431.1

Henderson, L. J., Gordon, R. G., & Engebretson, D. C. (1984). Mesozoic aseismic ridges on the Farallon Plate and southward migration of shallow subduction during the Laramide Orogeny. *Tectonics*, *3*(2), 121–132. https://doi.org/10.1029/TC003i002p00121

Hu, J., & Gurnis, M. (2020). Subduction Duration and Slab Dip. *Geochemistry, Geophysics, Geosystems*, *21*(4), 1–24. https://doi.org/10.1029/2019GC008862

Hu, J., & Liu, L. (2016). Abnormal seismological and magmatic processes controlled by the tearing South American flat slabs. *Earth and Planetary Science Letters*, *450*, 40–51. https://doi.org/10.1016/j.epsl.2016.06.019

Hu, J., Liu, L., Hermosillo, A., & Zhou, Q. (2016). Simulation of late Cenozoic South American flat-slab subduction using geodynamic models with data assimilation. *Earth and Planetary Science Letters*, *438*, 1–13. https://doi.org/10.1016/j.epsl.2016.01.011

Hu, J., Liu, L., Faccenda, M., Zhou, Q., Fischer, K. M., Marshak, S., & Lundstrom, C. (2018a). Modification of the Western Gondwana craton by plume–lithosphere interaction. *Nature Geoscience*, *11*(3), 203–210. https://doi.org/10.1038/s41561-018-0064-1

Hu, J., Liu, L., & Zhou, Q. (2018b). Reproducing past subduction and mantle flow using high-resolution global convection models. *Earth and Planetary Physics*, *2*(3), 189–207. https://doi.org/10.26464/epp2018019

Huangfu, P., Wang, Y., Cawood, P. A., Li, Z. H., Fan, W., & Gerya, T. V. (2016). Thermo-mechanical controls of flat subduction: Insights from numerical modeling. *Gondwana Research*, *40*, 170–183. https://doi.org/10.1016/j.gr.2016.08.012

van Hunen, J., van den Berg, A. P., & Vlaar, N. J. (2000). A thermo-mechanical model of horizontal subduction below an overriding plate. *Earth and Planetary Science Letters*, *182*(2), 157–169. https://doi.org/10.1016/S0012-821X(00)00240-5

van Hunen, J., van den Berg, A. P., & Vlaar, N. J. (2002). On the role of subducting oceanic plateaus in the development of shallow flat subduction. *Tectonophysics*, *352*(3–4), 317–333. https://doi.org/10.1016/S0040-1951(02)00263-9

van Hunen, J., van den Berg, A. P., & Vlaar, N. J. (2004). Various mechanisms to induce present-day shallow flat subduction and implications for the younger Earth: A numerical parameter study. *Physics of the Earth and Planetary Interiors*, *146*(1–2), 179–194. https://doi.org/10.1016/j.pepi.2003.07.027

Jones, C. (2012). Hydrodynamic mechanism for the Laramide orogeny. *Geosphere*, *7*(1), 183.

https://doi.org/10.1130/GES00575.1

Kapp, P., & Decelles, P. G. (2019). Mesozoic–Cenozoic geological evolution of the Himalayan-Tibetan orogen and working tectonic hypotheses. *American Journal of Science*, *319*(3), 159–254. https://doi.org/10.2475/03.2019.01

Li, C., van der Hilst, R. D., Meltzer, A. S., & Engdahl, E. R. (2008). Subduction of the Indian lithosphere beneath the Tibetan Plateau and Burma. *Earth and Planetary Science Letters*, *274*(1–2), 157–168. https://doi.org/10.1016/j.epsl.2008.07.016

Li, X. H. (2000). Cretaceous magmatism and lithospheric extension in Southeast China. *Journal of Asian Earth Sciences*, *18*(3), 293–305. https://doi.org/10.1016/S1367-9120(99)00060-7

Li, Y., Gao, M., & Wu, Q. (2014). Crustal thickness map of the Chinese mainland from teleseismic receiver functions. *Tectonophysics*, *611*, 51–60. https://doi.org/10.1016/j.tecto.2013.11.019

Li, Z. X., & Li, X. H. (2007). Formation of the 1300-km-wide intracontinental orogen and postorogenic magmatic province in Mesozoic South China: A flat-slab subduction model. *Geology*, *35*(2), 179–182. https://doi.org/10.1130/G23193A.1

Liu, J., Cai, R., Pearson, D. G., & Scott, J. M. (2019). Thinning and destruction of the lithospheric mantle root beneath the North China Craton: A review. *Earth-Science Reviews*, *196*(January), 102873. https://doi.org/10.1016/j.earscirev.2019.05.017

Liu, L. (2015). The ups and downs of North America: Evaluating the role of mantle dynamic topography since the Mesozoic. *Reviews of Geophysics*, *53*(3), 1022–1049. https://doi.org/10.1002/2015RG000489

Liu, L., & Stegman, D. R. (2011). Segmentation of the Farallon slab. *Earth and Planetary Science Letters*, *311*(1–2), 1–10. https://doi.org/10.1016/j.epsl.2011.09.027

Liu, L., Spasojević, S., & Gurnis, M. (2008). Reconstructing Farallon plate subduction beneath North America back to the Late Cretaceous. *Science*, *322*(5903), 934–938. https://doi.org/10.1126/science.1162921

Liu, L., Gurnis, M., Seton, M., Saleeby, J., Müller, R. D., & Jackson, J. M. (2010). The role of oceanic plateau subduction in the Laramide orogeny. *Nature Geoscience*, *3*(5), 353–357. https://doi.org/10.1038/ngeo829

Liu, L., Liu, L., & Xu, Y. G. (2021). Mesozoic intraplate tectonism of East Asia due to flat subduction of a composite terrane slab. *Earth-Science Reviews*, *214*(October 2020), 103505.

https://doi.org/10.1016/j.earscirev.2021.103505
Liu, M., Cui, X., & Liu, F. (2004). Cenozoic rifting and volcanism in eastern China: A mantle dynamic link to the Indo-Asian collision? *Tectonophysics*, *393*(1-4 SPEC.ISS.), 29–42. https://doi.org/10.1016/j.tecto.2004.07.029
Liu, S., & Currie, C. A. (2016). Farallon plate dynamics prior to the Laramide orogeny: Numerical models of flat subduction. *Tectonophysics*, *666*, 33–47. https://doi.org/10.1016/j.tecto.2015.10.010
Liu, S., Gurnis, M., Ma, P., & Zhang, B. (2017). Reconstruction of northeast Asian deformation integrated with western Pacific plate subduction since 200 Ma. *Earth-Science Reviews*, *175*(October), 114–142. https://doi.org/10.1016/j.earscirev.2017.10.012
Liu, Y., Liu, L., Wu, Z., Li, W., & Hao, X. (2020). New insight into East Asian tectonism since the late Mesozoic inferred from erratic inversions of NW-trending faulting within the Bohai Bay Basin. *Gondwana Research*, (xxxx). https://doi.org/10.1016/j.gr.2020.01.022
Ma, P., Liu, S., Gurnis, M., & Zhang, B. (2019). Slab Horizontal Subduction and Slab Tearing Beneath East Asia. *Geophysical Research Letters*, *46*(10), 5161–5169. https://doi.org/10.1029/2018GL081703
Manea, V. C., Pérez-Gussinyé, M., & Manea, M. (2012). Chilean flat slab subduction controlled by overriding plate thickness and trench rollback. *Geology*, *40*(1), 35–38. https://doi.org/10.1130/G32543.1
Mao, W., & Zhong, S. (2018). Slab stagnation due to a reduced viscosity layer beneath the mantle transition zone. *Nature Geoscience*, *11*(11), 876–881. https://doi.org/10.1038/s41561-018-0225-2
McNamara, A. K., & Zhong, S. (2004). Thermochemical structures within a spherical mantle: Superplumes or piles? *Journal of Geophysical Research: Solid Earth*, *109*(B7), 1–14. https://doi.org/10.1029/2003JB002847
Müller, R. D., Seton, M., Zahirovic, S., Williams, S. E., Matthews, K. J., Wright, N. M., et al. (2016). Ocean Basin Evolution and Global-Scale Plate Reorganization Events Since Pangea Breakup. *Annual Review of Earth and Planetary Sciences*, *44*(1), 107–138. https://doi.org/10.1146/annurev-earth-060115-012211
Müller, R. D., Zahirovic, S., Williams, S. E., Cannon, J., Seton, M., Bower, D. J., et al. (2019). A Global Plate Model Including Lithospheric Deformation Along Major Rifts and Orogens

Since the Triassic. *Tectonics*, *38*(6), 1884–1907. https://doi.org/10.1029/2018TC005462

Pang, Y., Guo, X., Zhang, X., Zhu, X., Hou, F., Wen, Z., & Han, Z. (2020). Late Mesozoic and Cenozoic tectono-thermal history and geodynamic implications of the Great Xing'an Range, NE China. *Journal of Asian Earth Sciences*, *189*(August 2019), 104155. https://doi.org/10.1016/j.jseaes.2019.104155

Qing, J. C., Ji, J. Q., Wang, J. D., Peng, Q. L., Niu, X. L., & Ge, Z. H. (2008). Apatite fission track study of Cenozoic uplifting and exhumation of Wutai Mountain, China. *Acta Geophysica Sinica*, *51*(2), 384–392. https://doi.org/10.1002/cjg2.1217

Saleeby, J. (2003). Segmentation of the Laramide Slab - Evidence from the southern Sierra Nevada region. *Bulletin of the Geological Society of America*, *115*(6), 655–668. https://doi.org/10.1130/0016-7606(2003)115<0655:SOTLSF>2.0.CO;2

Schellart, W. P. (2017). Andean mountain building and magmatic arc migration driven by subduction-induced whole mantle flow. *Nature Communications*, *8*(1), 1–13. https://doi.org/10.1038/s41467-017-01847-z

Schellart, W. P. (2020). Control of Subduction Zone Age and Size on Flat Slab Subduction. *Frontiers in Earth Science*, *8*(February), 1–18. https://doi.org/10.3389/feart.2020.00026

Schellart, W. P., Freeman, J., Stegman, D. R., Moresi, L., & May, D. (2007). Evolution and diversity of subduction zones controlled by slab width. *Nature*, *446*(7133), 308–311. https://doi.org/10.1038/nature05615

Seton, M., Müller, R. D., Zahirovic, S., Gaina, C., Torsvik, T., Shephard, G., et al. (2012). Global continental and ocean basin reconstructions since 200Ma. *Earth-Science Reviews*, *113*(3–4), 212–270. https://doi.org/10.1016/j.earscirev.2012.03.002

Song, Y., Ren, J., Stepashko, A. A., & Li, J. (2014). Post-rift geodynamics of the Songliao Basin, NE China: Origin and significance of T11 (Coniacian) unconformity. *Tectonophysics*, *634*, 1–18. https://doi.org/10.1016/j.tecto.2014.07.023

Stevenson, D. J., & Turner, J. S. (1977). Angle of subduction. *Nature*, *270*(5635), 334–336. https://doi.org/10.1038/270334a0

Sun, W., & Kennett, B. L. N. (2017). Mid-lithosphere discontinuities beneath the western and central North China Craton. *Geophysical Research Letters*, *44*(3), 1302–1310. https://doi.org/10.1002/2016GL071840

Tan, E., Choi, E., Thoutireddy, P., Gurnis, M., & Aivazis, M. (2006). GeoFramework: Coupling

multiple models of mantle convection within a computational framework. *Geochemistry, Geophysics, Geosystems*, *7*(6), 1–14. https://doi.org/10.1029/2005GC001155

Tang, J., Xu, W., Wang, F., & Ge, W. (2018). Subduction history of the Paleo-Pacific slab beneath Eurasian continent: Mesozoic-Paleogene magmatic records in Northeast Asia. *Science China Earth Sciences*, *61*(5), 527–559. https://doi.org/10.1007/s11430-017-9174-1

Torsvik, T. H., Steinberger, B., Shephard, G. E., Doubrovine, P. V., Gaina, C., Domeier, M., et al. (2019). Pacific-Panthalassic Reconstructions: Overview, Errata and the Way Forward. *Geochemistry, Geophysics, Geosystems*, *20*(7), 3659–3689. https://doi.org/10.1029/2019GC008402

Trumbull, R. B., Riller, U., Oncken, O., Scheuber, E., Munier, K., & Hongn, F. (2006). The Time-Space Distribution of Cenozoic Volcanism in the South-Central Andes: a New Data Compilation and Some Tectonic Implications. *The Andes*, 29–43. https://doi.org/10.1007/978-3-540-48684-8_2

Wu, F. Y., Yang, J. H., Xu, Y. G., Wilde, S. A., & Walker, R. J. (2019). Destruction of the north China craton in the mesozoic. *Annual Review of Earth and Planetary Sciences*, *47*, 173–195. https://doi.org/10.1146/annurev-earth-053018-060342

Xu, Y. G. (2001). Thermo-tectonic destruction of the archaean lithospheric keel beneath the Sino-Korean Craton in China: Evidence, timing and mechanism. *Physics and Chemistry of the Earth, Part A: Solid Earth and Geodesy*, *26*(9–10), 747–757. https://doi.org/10.1016/S1464-1895(01)00124-7

Xu, Y. G. (2007). Diachronous lithospheric thinning of the North China Craton and formation of the Daxin'anling-Taihangshan gravity lineament. *Lithos*, *96*(1–2), 281–298. https://doi.org/10.1016/j.lithos.2006.09.013

Zhang, J. H., Gao, S., Ge, W. C., Wu, F. Y., Yang, J. H., Wilde, S. A., & Li, M. (2010). Geochronology of the Mesozoic volcanic rocks in the Great Xing'an Range, northeastern China: Implications for subduction-induced delamination. *Chemical Geology*, *276*(3–4), 144–165. https://doi.org/10.1016/j.chemgeo.2010.05.013

Zhang, N., & Li, Z. X. (2018). Formation of mantle "lone plumes" in the global downwelling zone — A multiscale modelling of subduction-controlled plume generation beneath the South China Sea. *Tectonophysics*, *723*(November 2017), 1–13. https://doi.org/10.1016/j.tecto.2017.11.038

764 Zhang, R., Wu, Q., Sun, L., He, J., & Gao, Z. (2014). Crustal and lithospheric structure of
765 Northeast China from S-wave receiver functions. *Earth and Planetary Science Letters*, *401*,
766 196–205. https://doi.org/10.1016/j.epsl.2014.06.017
767 Zhang, X., Chung, S.-L., Lai, Y.-M., Ghani, A. A., Murtadha, S., Lee, H.-Y., & Hsu, C.-C.
768 (2019a). A 6000-km-long Neo-Tethyan arc system with coherent magmatic flare-ups and
769 lulls in South Asia. *Geology*, *47*(6), 573–576. https://doi.org/10.1130/G46172.1
770 Zhang, Y., Chen, L., Ai, Y., Jiang, M., Xu, W., & Shen, Z. (2018). Lithospheric structure of the
771 South China Block from S-receiver function. *Chinese Journal of Geophysics. (in Chinese)*,
772 *61*(1), 138–149. https://doi.org/10.6038/cjg2018L0226
773 Zhang, Y., Chen, L., Ai, Y., & Jiang, M. (2019b). Lithospheric structure beneath the central and
774 western North China Craton and adjacent regions from S-receiver function imaging.
775 *Geophysical Journal International*, *219*(1), 619–632. https://doi.org/10.1093/gji/ggz322
776 Zhong, S., McNamara, A., Tan, E., Moresi, L., & Gurnis, M. (2008). A benchmark study on
777 mantle convection in a 3-D spherical shell using CitcomS. *Geochemistry, Geophysics,*
778 *Geosystems*, *9*(10), 1–32. https://doi.org/10.1029/2008GC002048
779 Zhou, X. M., & Li, W. X. (2000). Origin of late mesozoic igneous rocks in Southeastern
780 China:Implications for lithosphere subduction and underplating of mafic magmas.
781 *Tectonophysics*, *326*(3–4), 269–287. https://doi.org/10.1016/S0040-1951(00)00120-7
782

783 **Acknowledgements**

784 This work is supported by NSF grant EAR1554554. The figures are prepared with GMT
785 (https://www.generic-mapping-tools.org/) and Paraview (https://www.paraview.org/). Surface
786 velocity and plate boundary files are exported using Gplates (https://www.gplates.org/). The
787 original version of CitcomS is available at www.geodynamics.org/cig/software/citcoms/. The P-
788 wave tomography model MIT-P08 is within the paper (Li et al., 2008) and its supporting
789 information.

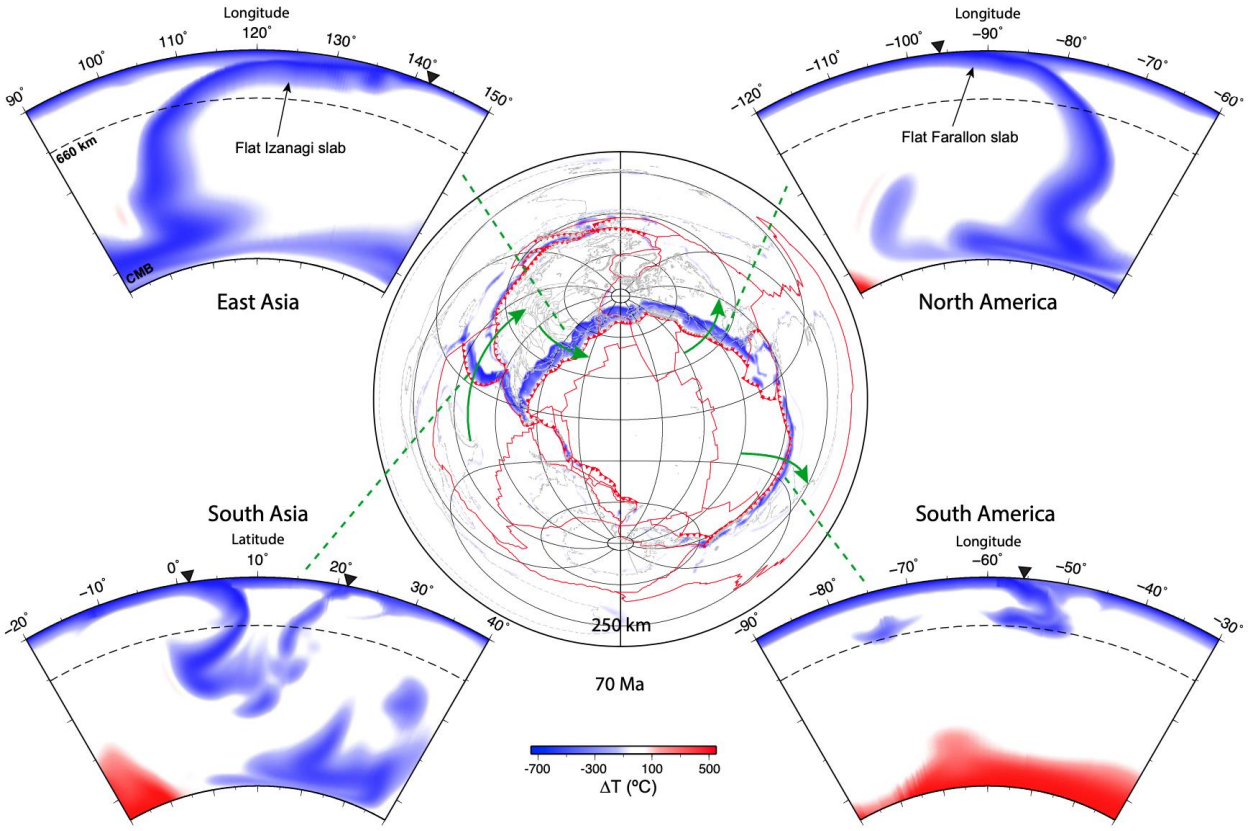

Figure 1. A global view of subducting slabs at 70 Ma from Model 1. The map in the center shows temperature at 250 km. The positions of the cross sections are marked on the map as green arrowed lines. The arrows on the map show the left-to-right direction of the cross sections. Along these major subduction zones, East Asia and North America had flat subduction during the Late Cretaceous, while the Tethyan and South American slabs were not.

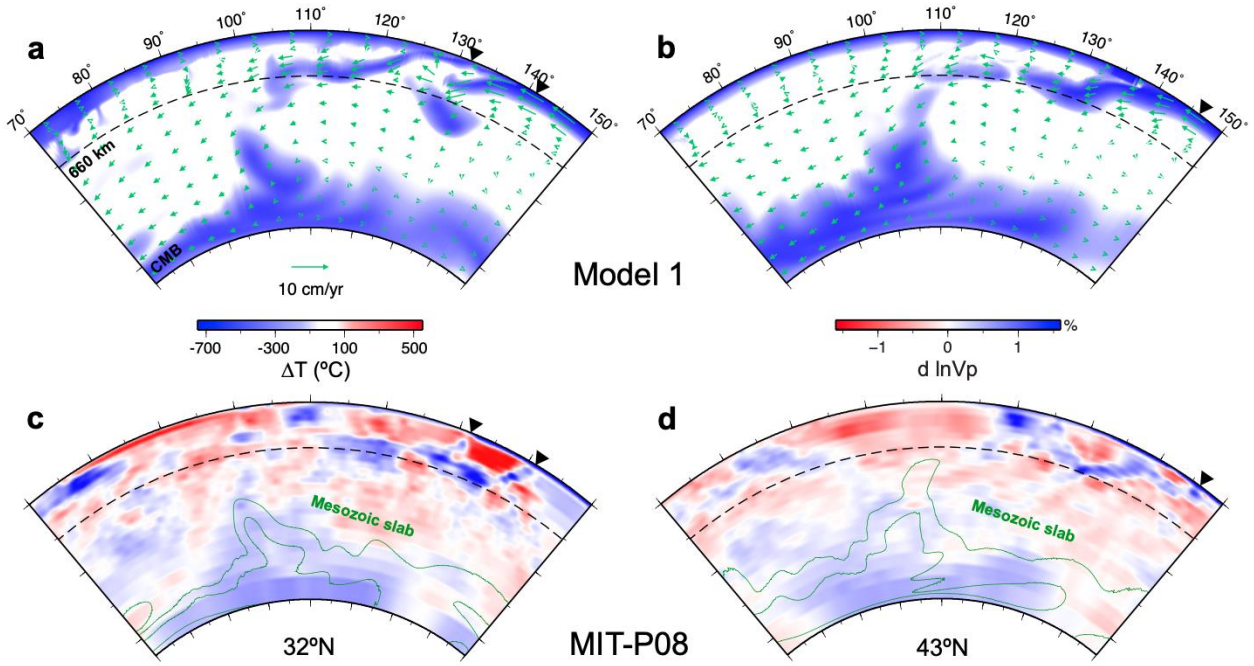

Figure 2. Model results vs. tomographic image for the present mantle structure. (a, b) Model predicted slab geometry and mantle flow at the present day along 32ºN and 43ºN, respectively. (c, d) P wave anomalies from the tomography MIT-P08 (Li et al., 2008) along 32ºN and 43ºN, respectively. The modeled lower-mantle slabs are mostly due to Mesozoic subduction, and are highlighted using green contours showing two different isotherms at 100 °C and 400 °C colder than the ambient mantle. Black triangles represent the present location of trenches. Note that the location and geometry of modeled lower-mantle slabs are consistent with those of the seismic image.

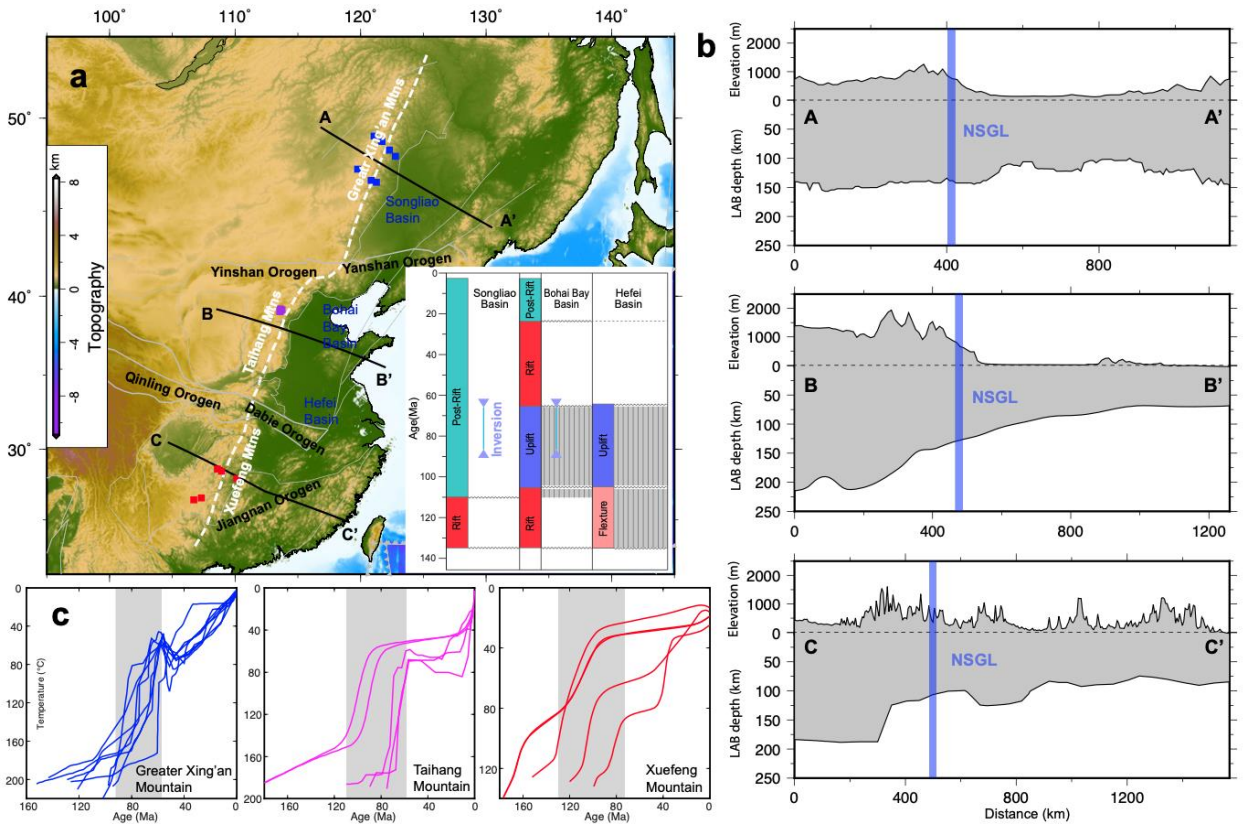

Figure 3. Geological constrains for the flat Izanagi subduction during the Late Cretaceous. (a) Topography of East Asia. The insert figure shows the evolution of Songliao Basin, Bohai Bay Basin and Hefei Basin. The gray column bars show the stratum loss. The period of basin inversion is marked by the magenta line. The NSGL (white dashed curve), which extends from Northeast China to South China, cuts the east-west trending tectonic belts including the Yinshan-Yanshan Orogen, Qinling-Dabie Orogen and Jiangnan Orogen. (b) The elevation and lithosphere-asthenosphere boundary (LAB) depth along AA', BB' and CC' (based on Zhang et al., 2014; Zhang et al., 2018; Zhang et al., 2019b), positions are marked in (a). To the eastern side of the NSGL, the elevation is lower, and LAB is shallower. (c) Thermochronology models for Greater Xing'an-Taihang-Xuefeng mountains (based on Clinkscales et al., 2020; Ge et al., 2016; Pang et al., 2020; Qing et al., 2008). The shaded zones show the time periods with major cooling events. At different locations, the time is consistent.

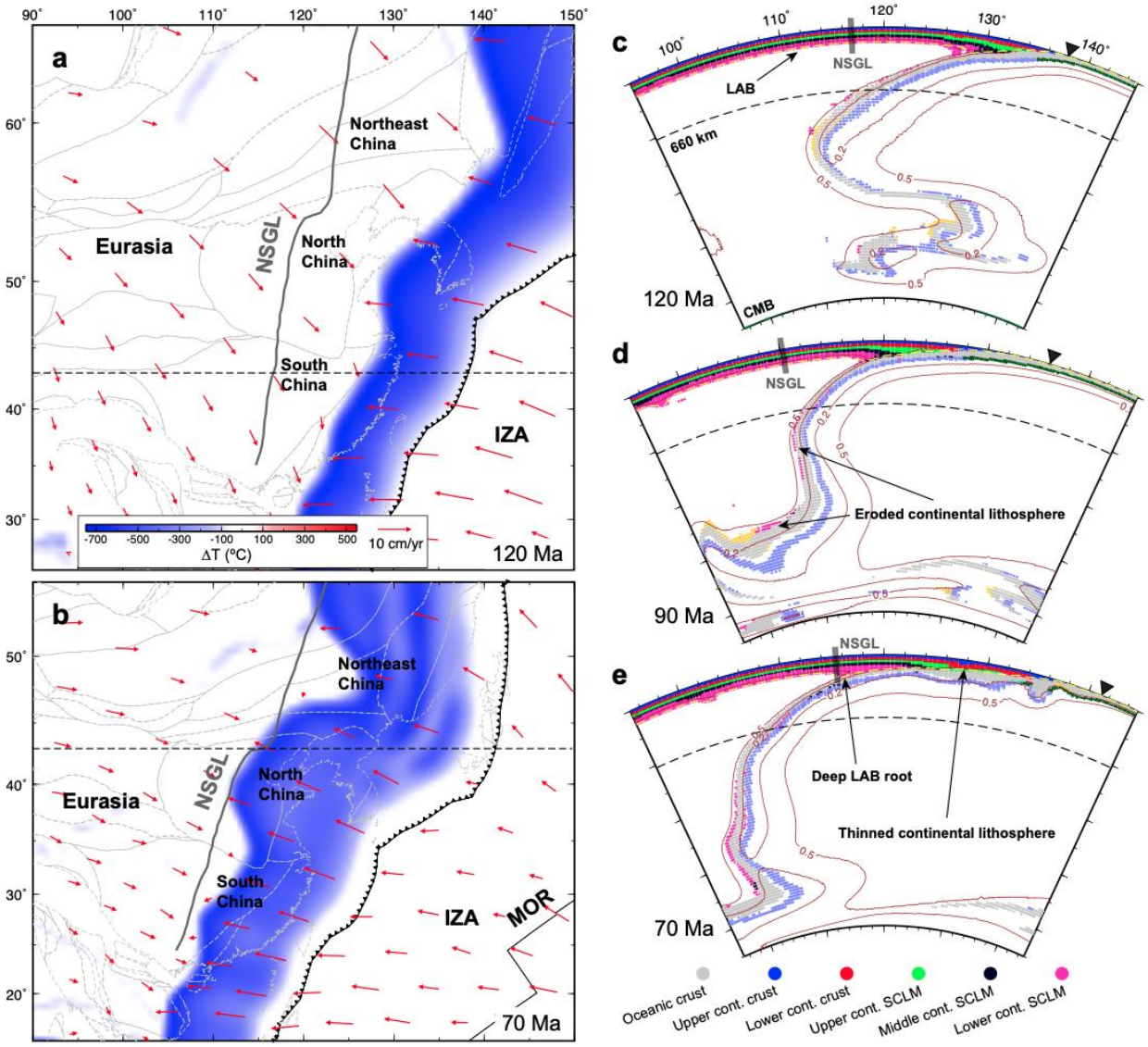

Figure 4. Evolution of the Izanagi slab and mantle flow in Model 1. (a, b) Map view at the depth of 250 km at 120 Ma and 70 Ma, respectively. The background temperature represents mantle temperature anomaly. Arrows represent mantle flow. The gray dashed lines show the locations of NSGL that are restored to the past following a plate reconstruction model (Müller et al., 2016). (c-e) Cross-sectional view of the compositional field along 43ºN at 120, 90 and 70 Ma, respectively. The contours show nondimensional temperatures of 0.2 and 0.5. Black triangles in (c-e) mark the trench locations. The gray bars show the NSGL locations.

827

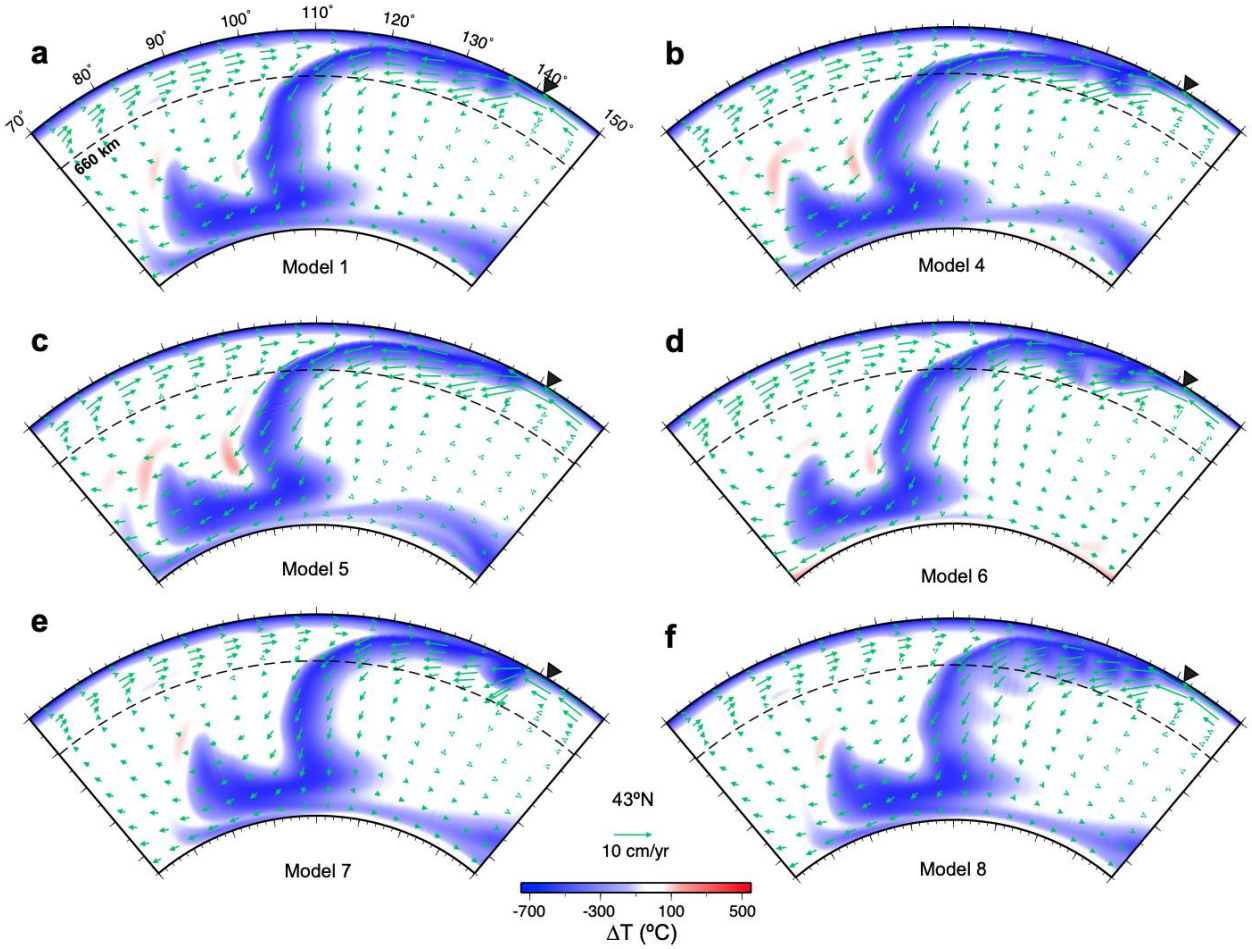

828

829 Figure 5. Slab geometries along 43ºN at 70 Ma in different models. Black triangles show trench
830 locations. Note that all these models have the flat Izanagi slab.

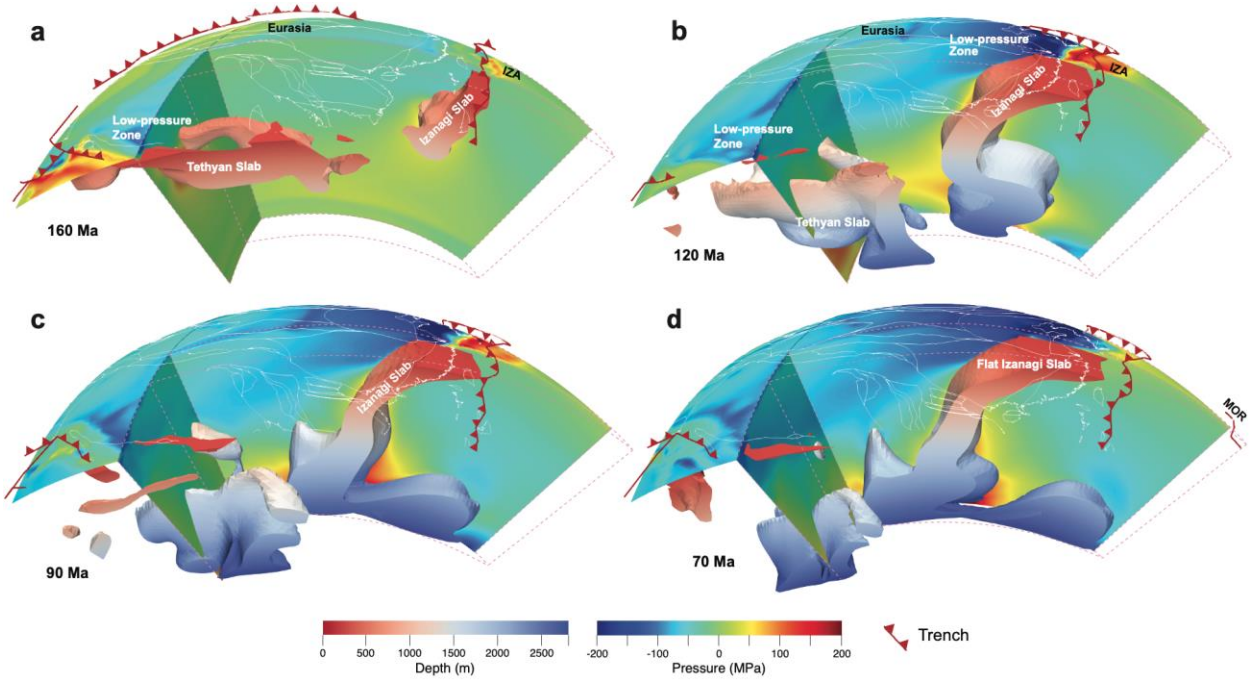

Figure 6. 3D view of the evolving dynamic pressure and slab geometry in Model 1. Slabs are shown as isovolumes with a non-dimensional temperature lower than 0.45, where the color of the slab represents depth, from 200 km to the CMB. On the spherical surface (at 100 km depth) and the vertical cross sections, color represents dynamic pressure. White curves show coastlines and tectonic provinces, while red curves show plate boundaries. Orange dash grid lines mark the position of several cross-sections that cut the Izanagi slab and dynamic pressure field.

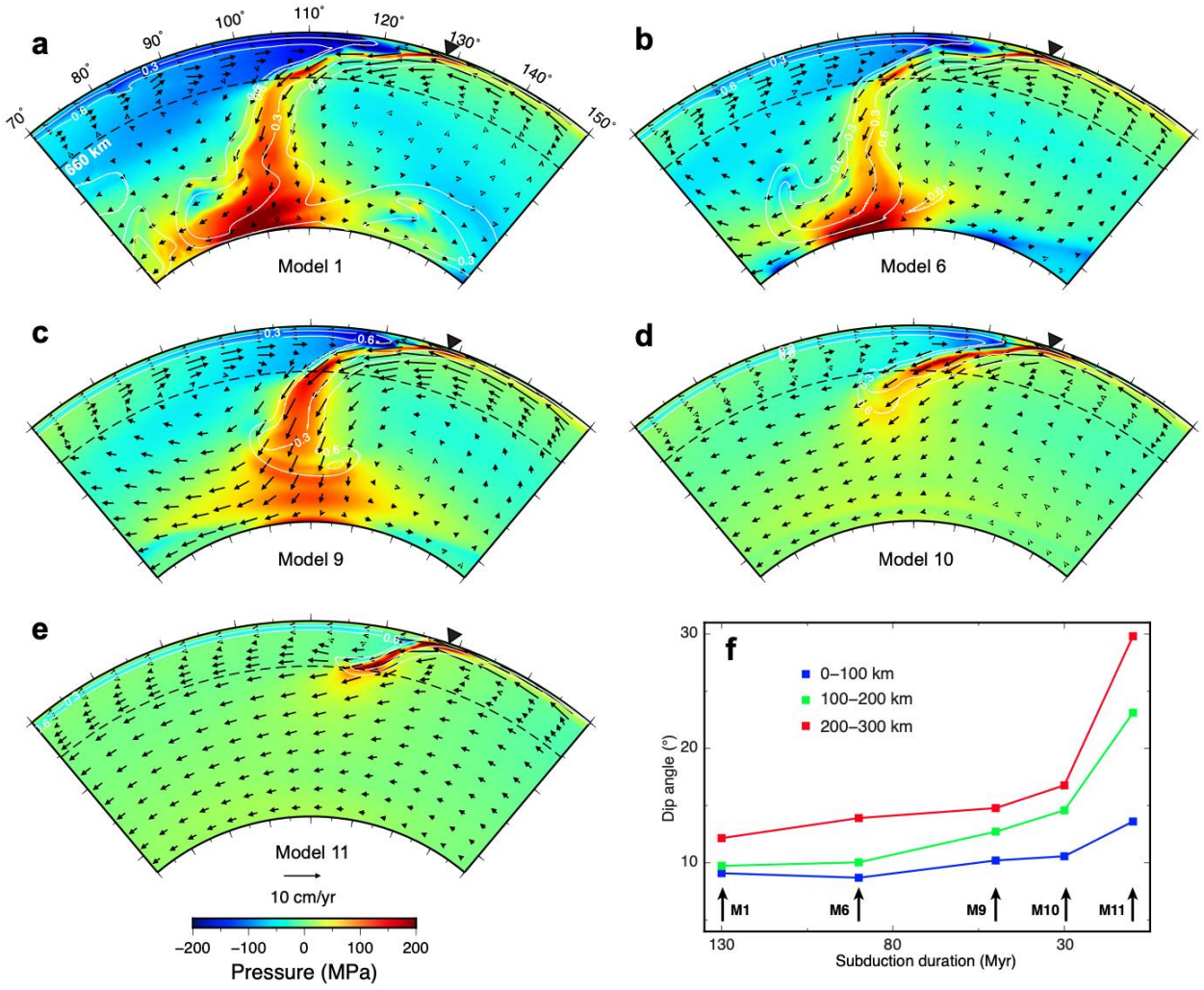

Figure 7. Variation of dynamic pressure and slab geometry with the starting age of subduction. (a-e) Distribution of dynamic pressure, mantle velocities and slabs along 32ºN in Models 1, 6 and 9-11, respectively. The two levels of white contours within the slab mark non-dimensional temperature at 0.3 and 0.6, respectively. Black triangles show trench locations. (f) Horizontally averaged slab dip for each model (M1 for Model 1) at three different depth intervals. Color-coded squares show the mean dip angle at given depth ranges.

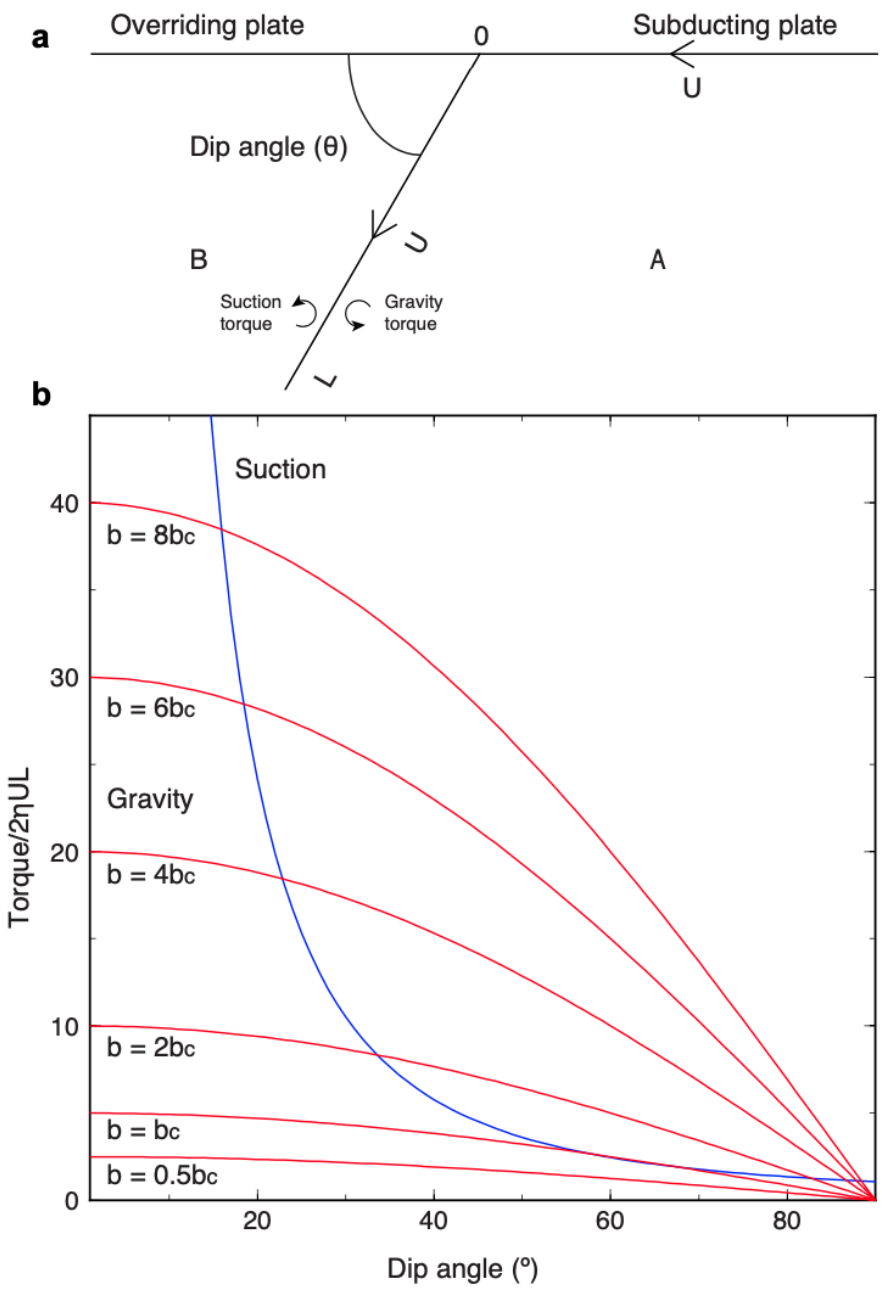

847

848 Figure 8. Slab torque balance and its effect on slab dip angle. (a) A simplified subduction system
849 with a fixed trench, a subduction rate of *U* and a slab length of *L*. Zone A and zone B experience
850 positive and negative dynamic pressure, forming a pressure-gradient across the slab. (b) The
851 balance between the suction torque (blue) and the gravity torque (red) as slab buoyancy (via *L*)
852 changes determines the slab dip angle. The critical slab dip and buoyancy are defined as when
853 there is only one solution in slab dip for the torque balance.

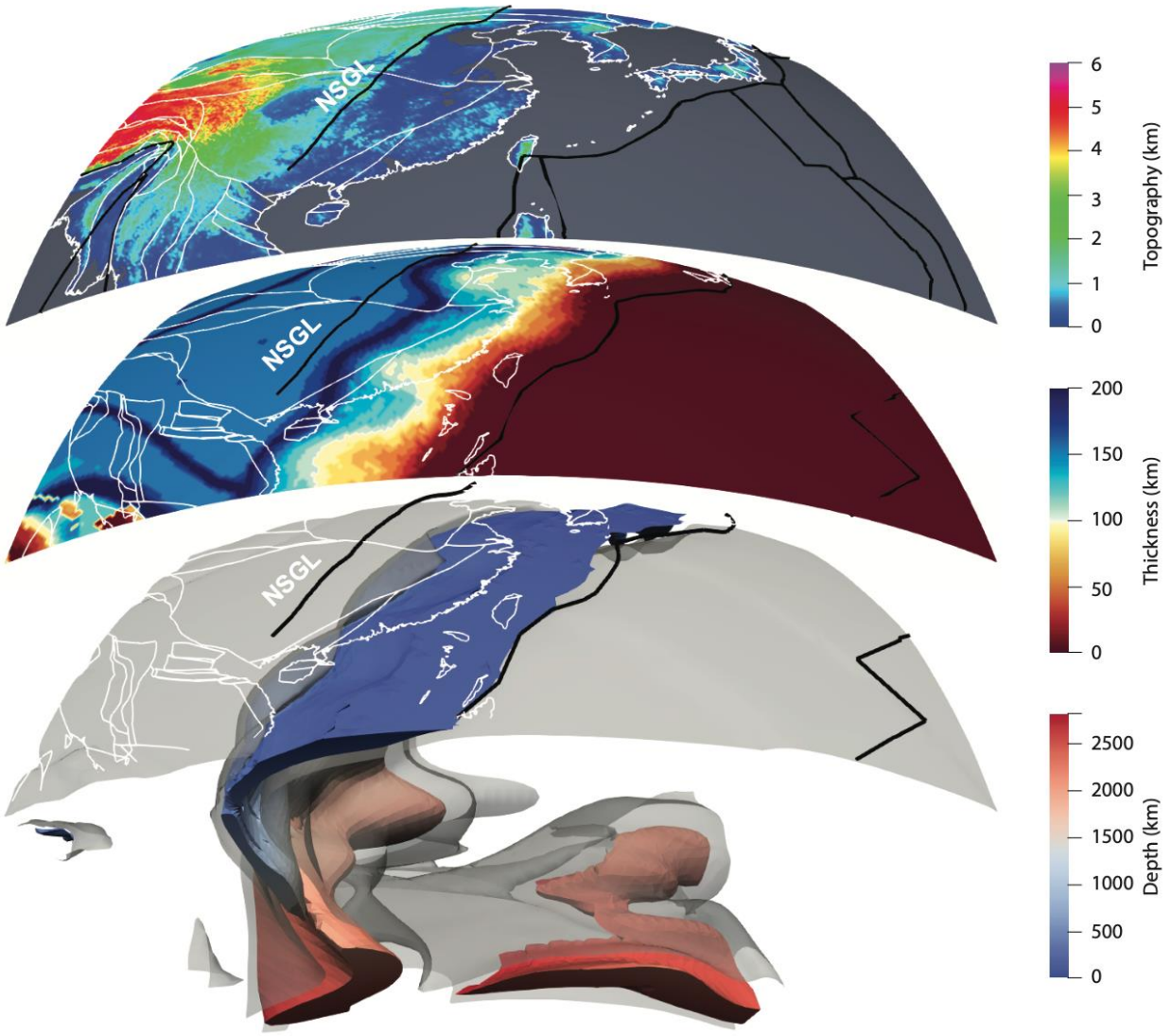

Figure 9. Flat slab, continental lithosphere thickness and topography. The slab geometry (bottom) and continental lithosphere thickness (middle) at 70 Ma are plotted against the present-day topography (top). The slab is shown as a volume at the inner part with the nondimensional temperature lower than 0.2 (color denoting slab depth) and an isosurfae of temperature at 0.45 at the outer part. Continental lithospheric thickness is calculated by tracing the composition of the lower lithosphere. The NSGL is shown as the thick black line. Plate boundaries (thick black lines), coastlines and tectonic outlines (thin white lines) were rotated following the continent based on plate kinematics (Müller et al., 2016) for comparison between 70 Ma and the present day.